Mathematical Models for Botanical Phenomena

Ann Bigelow, Emma Hayes, and Charlotte Moser

December 16, 2024

1 Introduction

In this project, we investigate three biochemically-motivated mathematical models for botanical phenomena. These models all reproduce patterns observed in plants which optimize energy usage.

Phyllotaxis, the arrangement of leaves, flowers, and florets on plants, is one important aspect of a plant's optimization of energy usage. Leonardo da Vinci noticed spirals in plants as early as 1452, and Charles Bonnet in 1754 found that these spirals were related to the golden ratio [1]. These spirals, whose formations are dependent on the golden angle, are very purposeful – they optimize leaf positioning and, thus, sunlight exposure.
Similarly, the positioning of root hairs in plant roots produce patterns which are advantageous in nature.

Figure 1: Spirals in a sunflower (Source).

These natural patterns beg for mathematical explanations. Fortunately, botanists and biologists have devised steadfast theories to explain these phenomena which has allowed impressive mathematical elucidation for botanical patterns.

To contribute to this fascinating field of study, in this report we focus on the numerical methods behind three successful mathematical models.

- Section 2 reproduces and builds upon results by Tanaka *et al.* from 2015. Tanaka approaches their model quite uniquely by considering the anatomy of the plant in comparatively more depth and ignoring any presence of a growth inhibitor – instead using existing leaves as inhibitors themselves.
  This paper does not mention any discretization choices, so we discuss our numerical approximation and the way in which we handled a unique delta function in the model. Because our simulation is computationally expensive, we also discuss program efficiency and timing.

- Section 3 discusses four methods to solve the activator-inhibitor model presented in Bernasconi *et al.* Bernasconi bases their model on the Gierer and Meinhardt kinetics discussed in [2], utilizing an activator and inhibitor chemical to initialize the growth of leaves. Ultimately, they wish to discover the golden angle in the space between points where a leaf would grow.

We attempt to reproduce results using both the methods discussed in the paper, and other suitable methods. We implement a Forward Euler scheme, two operator splitting methods utilizing Central Difference, Crank Nicolson, the fourth-order Runge Kutta Method, and Newton's Method.

- Lastly, section 4 explores three different methods to solve the Schnakenberg reaction diffusion model presented by Payne *et al.*. This model reproduces the development of a root hair on the cellular level. In this system we track the concentration of active and inactive proteins throughout the cell. The reaction kinetics in the Schnakenberg model are distinguished by a relatively simple non-linear auto and cross catalysis term.

  We implement Forward Euler, Crank Nicolson, and Spectral methods to solve this system and compare the run times of each method. We also note the role of the computationally expensive spectral method by giving an example of a closely related system whose dynamics cannot be reproduced by the simpler methods.

1.1 Spirals

Wilhelm Friedrich Benedikt Hofmeister, a giant in early biology and botany, wrote a book in 1868 that laid the foundation for the fundamental hypotheses used in mathematical models of phyllotaxis today [3]. His hypotheses fall broadly under an umbrella term, optimal packing (of leaves or florets). To understand Hofmeister's rules, it is necessary to describe the anatomy of a standard plant's stem (see figure 2). Much of our understanding of the anatomy was provided by Newell and Pennybacker [4], as well as Tanaka *et al.* [5].

An aerial view allows us to represent the stem of a plant as a series of concentric circles. The innermost circle is called the shoot apical meristem (SAM) and its boundary is referred to as the peripheral zone (PZ), which may be represented as ∂B_{R_0}, the boundary of the two-dimensional ball centered at (0,0) with radius R_0. The PZ is where clusters of cells, primordia, form and later become buds. As the plant grows upward, primordia twirl up and around, soon blooming into leaves.

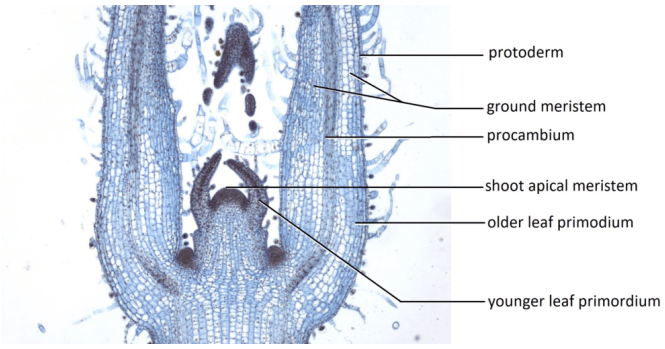

Figure 2: A plant stem with labeled meristem and primordia (Source)

Hofmeister roughly stated that primordia

1. form at constant time intervals along the PZ,
2. move radially outward, and
3. emerge in the **least crowded areas**

according to Newell and Pennybacker [4]. We found that there are two main schools of thought that mathematically describe these behaviors:

1. **The physical perspective**
   In 1996, Doaudy and Couder periodically dropped ferrofluid into circular dishes filled with oil. Magnetic repulsion between the drops caused them to navigate to the least crowded areas in the dish. Spiral patterns emerged and numerical simulations were produced to recreate this using a magnetic repulsive potential function [4, 5].

2. **The activator-inhibitor perspective**
   Auxin is a growth hormone in plants that acts as an activator for primordia formation in stems [6, 7]. A high concentration of auxin initiates the formation of primordia. After a primordium is formed, new primordia form as far away from the older formation as possible. This suggests the incorporation of a diffusion term in mathematical models.

Both perspectives produce biologically accurate results using and supporting Hofmeister's hypotheses. We focus on models showcasing the biochemical perspective, as the alternate view has been perceived to be quite simple [5].

Roger V. Jean's *A Systemic Study in Plant Morphogenesis* determines that the parastichy numbers are determined by the divergence angle, the angle between primordia. Parastichy numbers are the total observed number of spirals in plants, or parastichies. The counter-clockwise and clockwise parastichy numbers were observed by Jean to be consecutive terms in the Fibonacci or Lucas sequences 95% of the time in sunflowers.
After many primordia growths, the divergence angle converges to $\Phi = \frac{2\pi}{1+\phi}$ where $\phi = \frac{1+\sqrt{5}}{2}$ is the golden ratio.
This creates a very clear objective for mathematical models and can be attained via multiple approaches.

1.2 Root Hairs

We can also use activator-inhibitor models to describe the roots of plants. Plant roots have many tiny hairs. In fact, most of the surface area of the roots are the root hairs [9]. These hairs grow out of the epidermis of the root and are about 1 mm long and have a diameter between 10-20 μm [9].

In a root, cells line up along the epidermis with the youngest cell closest to the root tip. After formation, eventually the root hair cell begins to expand as the hair grows [9]. Most root cells have only one hair which develops at the basal end of the cell i.e. the far end from the root tip (see Figure 3) [8]. This produces regularly spaced hairs.

While this pattern has not been linked to the golden angle, it is still an interesting system to study since the placement of hairs is important for maximizing nutrient uptake [8].

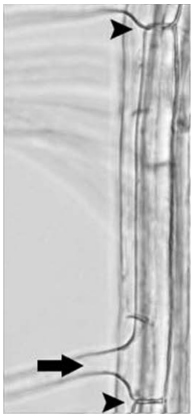

Figure 3: Picture of a root cell from [8]. The large arrow marks where the root hair is growing at the basal end of the cell. The smaller arrows indicate the ends of the cell.

2 Tanaka *et al.*

2.1 Auxin Transport: A Background for the Tanaka Model

Tanaka distinguishes between three layers within the peripheral zone of a plant's stem, labeled L1, L2, and L3. L1 is closest to the outside of the plant, and L3 is the innermost layer. *Auxin transport* describes the flow of the hormone between these layers and introduces the dual roles of auxin as both an activator and inhibitor.
Auxin transport is observed in a plant's stem in two primary capacities:

1. The *convergence of auxin flow* produces peaks of auxin in L1 and allows some models to neglect the distinction between layers in the PZ [5]. The Bernasconi system in section 3 is an example of this.

2. Basipetal transport is highlighted in Tanaka's model. This describes the one-way flow of auxin from L1 into L3. The general process is as follows:

   Auxin diffuses, decays, and is constantly produced in L1. Here, new primordia form where the auxin concentration is maximized. After a primordium is formed, auxin flows *away from* it and into L3 at a rate proportional to its total concentration in L1. This exhibits the "inhibitory effect" of existing primordia and auxin levels and reproduces Hofmeister's idea of optimal packing. The hormone is produced at a much higher rate in L3, and its concentration decays and diffuses at the same rate in both layers.

2.2 The Tanaka Model for Phyllotaxis

The final model used in our simulation describes the total concentration of auxin in L1 and L3. The model is given by the single partial differential equation

$$\epsilon \frac{\partial S_n}{\partial t} = D\Delta S_n - bS_n + a\sum_{j=0}^{n-1} \delta(\underline{x} - \underline{X_j(t)}) \tag{1}$$

for the n^{th} snapshot of auxin concentration S_n. Here, $\underline{x} \in \mathbb{R}^2$, $t \in ((n-1)T, nT)$, and T is the plastochron, the constant time interval between primordia formations. $X_j(t)$ tracks the positions of the old primordia, so that

$$X_j(t) = (R_0 + (t - jT)V)(\cos\theta_j, \sin\theta_j).$$

This expression captures the radially outward motions of primordia with radial velocity V beginning at $R_0 = 0.2$ mm. Additionally, Tanaka *et al.* enforce the "initial" condition

$$S_n(x, (n-1)T) = S_{n-1}(x, (n-1))T$$

which ensures that the total concentration of auxin throughout the domain is consistent between plastochron T.
The remaining parameters are listed below.

- $\epsilon = 0.1$ balances the very small diffusion coefficient $D = 3.47 \times 10^{-6}$ mm^{2}s^{-1} and decay rate $b = 1.39 \times 10^{-3}$ s^{-1} with a long plastochron of $T = 7200$ s.
- a is the rate on the term $\sum_{j=0}^{n-1} \delta(x - X_j(t))$. This enforces a peak in auxin concentration at the locations of existing primordia.

We used the initial conditions provided in Tanaka's paper:

$$\theta_0 = 0;\ \theta_1 = \pi;\ S_1(r, \theta) = 0.$$

We solve for S_n for each $nT,\ n = 2, 3, 4, \ldots$. The boundary conditions we used are

$$S_n(r, 0) = S_n(r, 2\pi); \quad S_n(r, \theta) = 0 \text{ for } r < 0.2 \text{ mm and } r > 5 + 0.2 \text{ mm}$$

because these seemed the most intuitive. At each n, S_n is minimized on ∂B_{R_0} to find θ_n. Notably, minimizers of S_n correspond with maximizers of S_n^1, the auxin concentration in L1, on ∂B_{R_0}. The divergence angle

$$\phi_n = \theta_n - \theta_{n-1}$$

converges to the golden angle as n becomes large, as discussed in section 2.5.

2.3 Mechanisms Behind the Tanaka Model

Equation (1) is a combined version of the following equations, which more clearly describe the mechanisms behind phyllotaxis. The equations are

$$\epsilon \frac{\partial S_n^1}{\partial t} = D\Delta S_n^1 - bS_n^1 - \beta(S_n^1)|S_n^3 - S_n^1|\chi_{A_n} + p; \tag{2}$$

$$\epsilon \frac{\partial S_n^3}{\partial t} = D\Delta S_n^3 - bS_n^3 + \beta(S_n^1)|S_n^3 - S_n^1|\chi_{A_n} + a\sum_{j=0}^{n-1} \delta(\underline{x} - \underline{X_j(t)}). \tag{3}$$

New primordia form at

$$\theta_n^1 = \max_{\theta} S_n^1(R_0, \theta).$$

As discussed above, in practice we solve a *minimization* problem for S_n.
This system describes the concentration of auxin in L1 and L3, S_n^1 and S_n^3, respectively. There are several additional terms in this original version of Tanaka's model:

- Importantly, the equations impose a constant source of auxin in L1 by adding p. Richard Smith *et al.* [7] legitimized this constant source.
- $\beta(S_n^1)$ is a function dependent on S_n^1 and represents the rate of basipetal transport. Thus,

$$-\beta(S_n^1)|S_n^3 - S_n^1|\chi_{A_n}$$

is the basipetal transport term. The basipetal transport is a one-way transport from L1 to L3. Tanaka *et al.* define the characteristic function χ_{A_n} to be

$$\chi_{A_n} = \begin{cases} 1, & x \in A_n \\ 0, & x \notin A_n \end{cases}$$

for $A_n = \bigcup_{j=0}^{n-1} B(X_j(t), r)$. Physically, this term simulates the fact that basipetal transport occurs only in neighborhoods of existing primordia. The size of the neighborhood around X_j is unspecified, but is irrelevant in the final model in 1.

- Because auxin is produced at a higher rate in L3 [7], the delta term is only present in the second equation.

Adding 2 and 3 produces another PDE for the total concentration $\bar{S_n}$ throughout both layers. Defining

$$S_n := \bar{S_n} - \tfrac{p}{b}$$

produces the final equation in (1).

2.4 Numerical Method

We chose to discretize (1) in polar coordinates to best represent the domain. The Laplace operator in polar coordinates is

$$\nabla^2 = \frac{\partial^2}{\partial r^2} + \frac{1}{r}\frac{\partial}{\partial r} + \frac{1}{r^2}\frac{\partial^2}{\partial \theta^2}.$$

In the numerical simulation, we use the standard centered-difference approximations for the derivative terms in the PDE in (1). The full discretization for the n^{th} concentration field S_n (n is removed for simplicity) is

$$\epsilon\left(\frac{S_{i,l}^{m+1} - S_{i,l}^{m}}{k}\right) = D[\nabla^2 S^m] - bS^m + A(\underline{x}) \tag{4}$$

for

$$\nabla^2 S^m = \frac{S_{i+1,l}^m - 2S_{i,l}^m + S_{i-1,l}^m}{h_r^2} + \frac{1}{r_i}\left(\frac{S_{i+1,l}^m - S_{i-1,l}^m}{2h_r}\right) + \frac{1}{r_i^2}\left(\frac{S_{i,l+1}^m - 2S_{i,l}^m + S_{i,l-1}^m}{h_\theta^2}\right)$$

and $h_r = \frac{5\text{mm}}{N}$, $h_\theta = \frac{2\pi}{N}$, and a grid size of N. The value $h_r = \frac{5\text{mm}}{N}$ was chosen to approximate an arbitrary plant's stem size as $5 + R_0$ mm.
For each plastochron T, T/k timesteps (indexed by m) are taken where $k = h_r/3$. A larger timestep caused a stability issue in the simulation. In the future, it would be informative to find this stability restriction rigorously. Additionally, we define

$$A(\underline{x}) = a\sum_{j=0}^{n-1} \delta(\underline{x} - \underline{X_j(t)}); \;\; \delta(\underline{x} - \underline{X_j(t)}) = \begin{cases} 1/A_s & |r_j - r| \le \frac{h_r}{2} \text{ and } |\theta_j - \theta| \le \frac{h_\theta}{2} \\ 0 & \text{otherwise} \end{cases}$$

where $\underline{X_j} = r_j(\cos\theta_j, \sin\theta_j)$ and $\underline{x} = r(\cos\theta, \sin\theta)$. This definition allows for a proper δ function with an approximate integral value of one. The area of the annulus sector with inner radius $r_j - \frac{h_r}{2}$, outer radius $r_j + \frac{h_r}{2}$ and angle h_θ is

$$\begin{aligned} A_s &= \frac{h_\theta}{2}\left(r_j + \frac{h_r}{2}\right)^2 - \frac{h_\theta}{2}\left(r_j - \frac{h_r}{2}\right)^2 \\ &= h_\theta h_r r_j. \end{aligned}$$

This comes from the area of the sector of a circle with angle θ and radius r,

$$A = \tfrac{\theta}{2} r^2.$$

Figure 4 is a cartoon that visualizes this.

In the code, S^m is represented as an $N \times N$ matrix storing the concentration levels at the i^{th} radius between $R_0 = 0.2$ mm and $R_0 + 5$ mm and l^{th} angle between 0 and 2π. After each plastochron we search for the smallest element of S_n in its first row, ∂B_{R_0}. This element corresponds with θ_n.

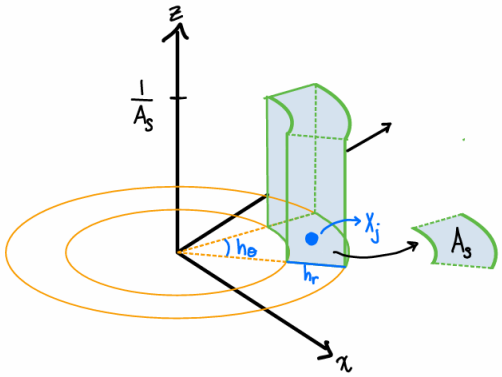

Figure 4: The Sector of the Annulus Centered around X_j which Defines the Delta Term in the Tanaka PDE

This process was repeated up to $n = 200$, for a total of

$$(T/k = 388,800) \times ((n = 200) - 1) = 77,371,200 \text{ timesteps}$$

when $N = 90$.

2.5 Results

The Convergence of the Divergence Angle

Figure 5 illustrates the convergence of the divergence angle as $n \to 100$. We noticed that the number of grid points N had to be at least ninety for ϕ_n to converge as $n \to \infty$. In fact, we see that ϕ_n actually approaches an angular value that is not precisely $\Phi = \frac{2\pi}{1+\phi}$, likely because the spacing should be made even smaller.

Additionally, for various versions of the code `theta_convergence.m` the values of θ_n were set to be $2\pi - \theta_n$ in order to observe convergence. This likely had to be done because there is some nuance in the minimizing value of S_n – as discussed in [5], this extremum is not unique for most n.

The Spiral

Figure 6 includes four snapshots from the movie `spiral_movie_n100.avi`. This movie assigns a color to each primordium X_n for $n = 0, 1, \ldots, 100$, and tracks them for the time stamps $t = 0T, T, \ldots, 100T$ seconds.

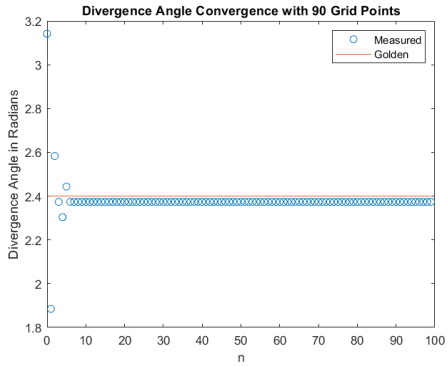

Figure 5: The Convergence of the Divergence Angle from the Tanaka Model as $n \to 100$

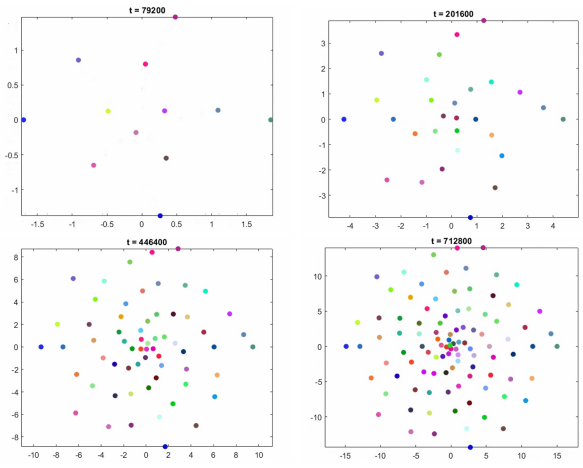

Figure 6: Four Snapshots of the Spiral Movie

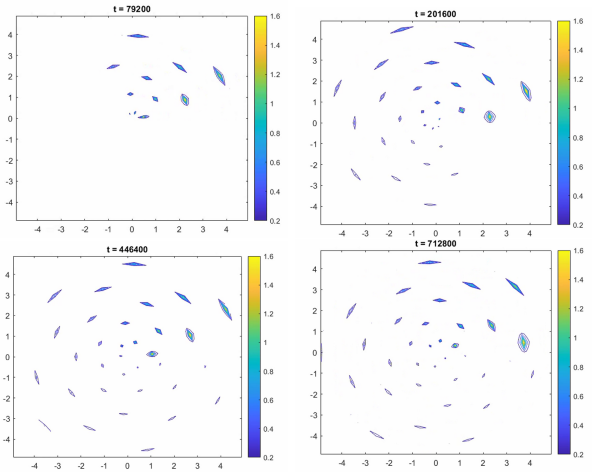

Figure 7: Four Snapshots of the Auxin Concentration Movie

Note that this movie was created with $N = 50$ for higher speed and the axes stretch beyond $r = R_0 + 5$ mm, the radius of the plant, although they should be cut off. We chose not to do this only because the growing spiral is mesmerizing.

In addition to capturing the locations of the primordia, we also created a movie (`S_movie_n100.avi`) using snapshots of contours of the auxin concentration S_n for the same time stamps, as seen in figure 7. The movie captures the diffusion of the auxin and its peaks at old primordia positions.

Timing

On a laptop with four cores, the programs were expensive due to our very large value of $T/k = 388,800$ when $N = 90$. An especially instructive aspect of this project was learning to refine our programming skills. The timing results of the solver `Tanaka_Solver.m` in MATLAB after vectorizing and changing the grid size were interesting. Figure 8 proves that avoiding large loops-within-loops *and* vectorizing calculations where possible is significantly more efficient. A version of the code is available in C++ as well, but was observed to be less efficient. This could be improved.

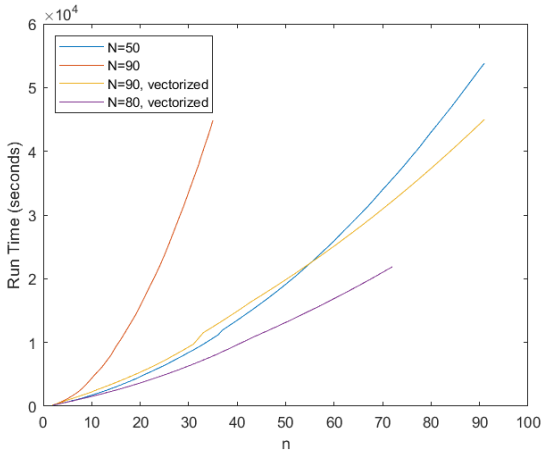

Figure 8: Comparison of the Wall-Clock Times for Various Versions of the MATLAB Tanaka Solver

3 Reaction Diffusion: Bernasconi

3.1 Introduction

Symmetry breaking is a process in which a certain symmetry or uniformity is broken in order for a more structured, but possibly less symmetric state to come about. This phenomenon marks the beginning of a self-organizing process that is prevalent in morphogenesis and biology as a whole. A natural question to ask, then, is without a pattern already present in a system or any external factors, can a physical system give rise to a pattern characterized by broken symmetry on its own? Alan Turing was the first to consider this problem in a reaction-diffusion model, with two chemicals reacting and diffusing. He emphasized that allowing the chemicals to diffuse would make it possible for broken symmetry to occur. Since then, many activator-inhibitor models have been studied and, in particular, Bernasconi *et al.* [10] build upon the Gierer and Meinhardt kinetics [2], and the Scholz model [11]. The Scholz model shows the peaks in an activator shifting by an angle δ on a ring representing a stem over time. That angle δ turns out to converge close to the golden angle.

Bernasconi *et al.* present a model for a reaction-diffusion system with three chemical substances, an activator, an inhibitor, and a source. This system exhibits spontaneous symmetry breaking and models a mechanism of phyllotaxis. They find regular, time-periodic solutions, motivated by a slight perturbation in the activator only.

3.2 Activator-Inhibitor Model

This model consists of three coupled PDEs in one time and one space dimension. There is an equation for the activator, a, the inhibitor, h, and the source, s. The source is an addition Bernasconi makes to the Gierer-Meinhardt model to act as a chemical memory for the system. The space domain is a unitary ring, allowing us to focus on a vector from 0 to 1 with periodic boundary conditions. The time domain is unspecified, but we will be looking at times of up to 50 seconds.

$$\begin{aligned}
\frac{\partial a}{\partial t}(x,t) &= \frac{a^2(x,t)}{h(x,t)} - \mu a(x,t) + \rho + d_a \frac{\partial^2 a}{\partial x^2}(x,t) \\
\frac{\partial h}{\partial t}(x,t) &= a^2(x,t) - \nu h(x,t) + \epsilon s(x,t) + d_h \frac{\partial^2 h}{\partial x^2} \\
\frac{\partial s}{\partial t}(x,t) &= a(x,t) - \kappa s(x,t) + d_s \frac{\partial^2 s}{\partial x^2}(x,t)
\end{aligned} \tag{5}$$

Parameter	Meaning	Value
μ	decay rate of the activator	30
ν	decay rate of the inhibitor	20
ρ	homogeneous activator source	1
κ	decay rate of the source	0.8
ϵ	links source to inhibitor	0.4
d_a	activator diffusion coefficient	0.050
d_h	inhibitor diffusion coefficient	0.300
d_s	source diffusion coefficient	0.001

Table 1: Parameters, their meaning, and their values from [10] for (5)

Computing the Initial Values: Bernasconi explicitly gives the initial values they chose for the activator concentration:

$$a(t=0, x=0.4) = 0.270, \quad a(t=0, x=0.7) = 0.268, \quad a(t=0, x) = 0.263.$$

They then say that the initial profile for the inhibitor and the source are the homogeneous profiles of the fixed point, meaning we must compute them using $a - \kappa s = 0$ for the source, and $a^2 - \nu h + \epsilon s = 0$ for the inhibitor. Bernasconi also mentions that only the activator has been perturbed. Thus, our initial values for the source and inhibitor are:

$$s(t=0, x) = 0.3287, \quad h(t=0, x) = 0.0100.$$

3.3 Numerical Methods

3.3.1 Forward Euler

We will begin with a simple forward Euler scheme, which utilizes a forward Euler step for the time derivative, and a second order centered difference method for the second spacial derivative. We do see that this system of PDEs is a nonlinear system, though, so this scheme may be unstable and prove to be inaccurate. We expand upon this further in the results of this section.

First we will implement our forward Euler scheme for the activator (A), which is dependent on the previous iteration or both itself and the inhibitor (H). Note that $\mathbb{I}$ is the identity matrix, and $\mathbb{D}$ is the centered difference second derivative matrix, both with periodic boundary conditions.

$$\begin{aligned}
&\frac{A_j^{n+1} - A_j^n}{\Delta t} = \rho + \frac{(A_j^n)^2}{H_j^n} - \mu A_j^n + d_a \frac{A_{j-1}^n - 2A_j^n + A_{j+1}^n}{(\Delta x)^2} \\
&\implies A_j^{n+1} = \Delta t \rho + \Delta t \frac{(A_j^n)^2}{H_j^n} + \left[(1 - \Delta t \mu)\mathbb{I} + \Delta t d_a \mathbb{D}\right] A_j^n
\end{aligned} \tag{6}$$

Next, our inhibitor (H), depends on previous steps of itself, the activator (A), and the source (S):

$$\begin{aligned} \frac{H_j^{n+1} - H_j^n}{\Delta t} &= (A_j^n)^2 - \nu H_j^n + \epsilon S_j^n + d_h \frac{H_{j-1}^n - 2H_j^n + H_{j+1}^n}{(\Delta x)^2} \\ \implies H_j^{n+1} &= \Delta t (A_j^n)^2 + \Delta t \epsilon S_j^n + \left[(1 - \Delta t \nu)\mathbb{I} + \Delta t d_h \mathbb{D}\right] H_j^n \end{aligned} \tag{7}$$

Finally, our source (S), depends on previous steps of itself and the activator (A):

$$\begin{aligned} \frac{S_j^{n+1} - S_j^n}{\Delta t} &= A_j^n - \kappa S_j^n + d_s \frac{S_{j-1}^n - 2S_j^n + S_{j+1}^n}{(\Delta x)^2} \\ \implies S_j^{n+1} &= \Delta t A_j^n + \left[(1 - \Delta t \kappa)\mathbb{I} + \Delta t d_s \mathbb{D}\right] S_j^n \end{aligned} \tag{8}$$

3.3.2 Operator Splitting

These PDEs lend themselves well to being split into their reaction and diffusion components. Indeed, the original authors of the paper even make reference to handling the diffusion separately and implementing an RK4 scheme to handle time-stepping reaction. Thus, we have done the same.

Diffusion

We first do the diffusion step, then use that result to compute the reaction step. We implemented two methods to handle the diffusion term: a simple central difference scheme, and the Crank-Nicolson method. The central difference is:

$$\frac{\partial^2 u}{\partial x^2} = d_u \frac{u_{j-1}^n - 2u_j^n + u_{j+1}^n}{(\Delta x)^2} \tag{9}$$

The Crank-Nicolson scheme involves both u^n and u^{n+1} terms, so we must begin with,

$$u^{n+1} = u^n + d_u \mathbb{D} \frac{u^{n+1} + u^n}{2(\Delta t)^2} \tag{10}$$

and move the u^{n+1} terms together to get

$$u^{n+1} = \left(\mathbb{I} - \frac{d_u}{2(\Delta t)^2}\mathbb{D}\right)^{-1} \left(\mathbb{I} + \frac{d_u}{2(\Delta t)^2}\mathbb{D}\right) u^n \tag{11}$$

Reaction

We implement an RK4 scheme for the reaction parts of each:

$$\frac{\partial a}{\partial t} = \frac{a^2}{h} - \mu a + \rho, \qquad \frac{\partial h}{\partial t} = a^2 - \nu h + \epsilon s, \qquad \frac{\partial s}{\partial t} = a - \kappa s$$

$$
\begin{aligned}
\frac{\partial u}{\partial t} &= f(u,t) \\
k_1 &= \Delta t f(u_n, t_n) \\
k_2 &= \Delta t f(u_n + \frac{k_1}{2}, t_n + \frac{\Delta t}{2}) \\
k_3 &= \Delta t f(u_n + \frac{k_2}{2}, t_n + \frac{\Delta t}{2}) \\
k_4 &= \Delta t f(u_n + k_3, t_n + \Delta t) \\
u^{n+1} &= u^n + \frac{1}{6}(k_1 + 2k_2 + 2k_3 + k_4)
\end{aligned} \tag{12}
$$

3.3.3 Newton's Method

Since this is a system of nonlinear PDEs, we need to choose an appropriate method, such as Newton's method. This requires us to compute the Jacobian of the root function found from (5). Multiple attempts to solve this problem were made, the most recent of which can be found in the GitHub repository for this project. Unfortunately, the Jacobian computed becomes singular after a certain number of iterations, indicating something is wrong with the method in its current form. Nevertheless, we first need to define the function we are finding the roots of:

$$
\begin{aligned}
F([a,h,s]) = \big[& -3a_j^n + 4a_j^{n-1} - a_j^{n-2} + 2dt \left(\frac{(a_j^n)^2}{h_j^n} - \mu a_j^n + \rho + d_a \frac{a_{j+1}^n - 2a_j^n + a_{j-1}^n}{dx^2} \right), \\
& -3h_j^n + 4h_j^{n-1} - h_j^{n-2} + 2dt \left((a_j^n)^2 - \nu h_j^n + \epsilon s_j^n + d_h \frac{h_{j+1}^n - 2h_j^n + h_j^n}{dx^2} \right), \\
& -3s_j^n + 4s_j^{n-1} - s_j^{n-2} + 2dt \left(a_j^n - \kappa s_j^n + d_s \frac{s_{j+1}^n - 2s_j^n + s_j^n}{dx^2} \right) \big]
\end{aligned} \tag{13}
$$

Notice that the U_j^{n-1} and U_j^{n-2} terms are considered constants in this vector, so when we compute the Jacobian they simply disappear. The Jacobian of this function is a $3N \times 3N$ block matrix, with blocks corresponding to the partial derivatives of each component of F:

$$
J_F([a,h,s]) = \begin{pmatrix}
-3 + 2dt(\frac{2a^n}{h^n} - \mu + d_a(\mathbb{D})^2) & -2dt\frac{(a^n)^2}{(h^n)^2} & 0 \\
4dta^n & -3 + 2dt(-\nu + d_h(\mathbb{D})^2) & 2dt\epsilon \\
2dt & 0 & -3 + 2dt(-\kappa + d_s(\mathbb{D})^2)
\end{pmatrix}
$$

3.4 Results

First, we can see how each of the methods model the concentration of the activator, inhibitor, and source over time. In Figure 9 we graph these predictions over all time at the x=1 point on the ring.

We can see that both RK4 schemes converge very quickly to consistent concentration peaks, but the forward Euler scheme does not seem to converge to a specific solution even over a much larger time (50 seconds vs 25 seconds). For each of these methods, we used a time step of 0.001

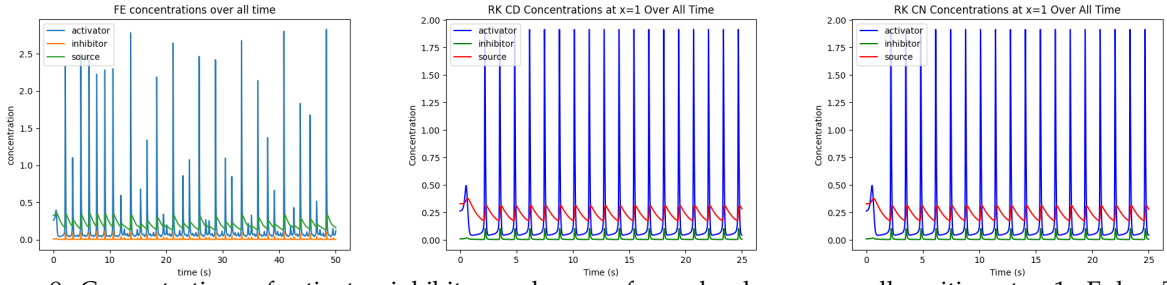

Figure 9: Concentrations of activator, inhibitor, and source for each scheme over all position at x=1. Euler: T=50, dt=0.0001, dx=0.01 ; RK4 CD: T=25, dt=0.0001, dx=0.01 ; RK4 CN: T=25, dt=0.0001, dx=0.01

and a space step of 0.01 to avoid any stability issues. However, later on we will analyze the RK4 schemes with a much smaller time interval and a smaller space step to refine our grid and hopefully get more accurate results. The behavior of the RK4 schemes seems to be more aligned with the expected behavior as shown in Bernasconi [10].

Next, we wished to show the period of the activator concentration peaks. In Figure 10 we graph the period, the time between each consecutive activator peak, over the entire time interval for each scheme.

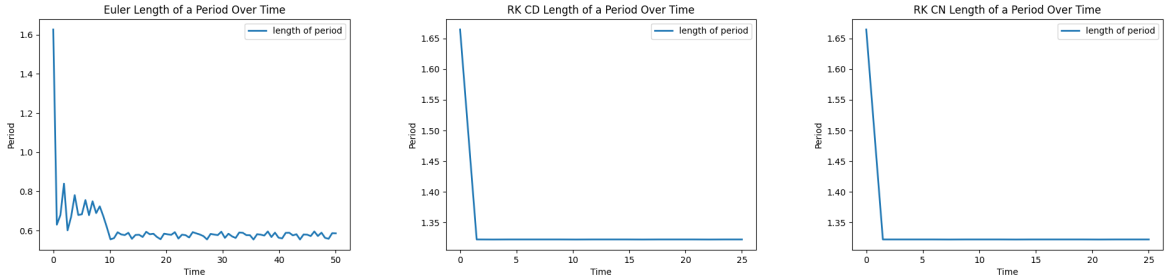

Figure 10: Convergence to a period for each scheme over time. Euler: 0.56-0.58; RK4 CD: 1.32; RK4 CN: 1.32

We can see that each scheme was able to roughly converge to a period, with each RK4 scheme agreeing on the period. Interestingly, the period the RK4 schemes converge to is 1.32 seconds, which Bernasconi records as the period before implementing diffusion (so that each diffusion coefficient is equal to zero). One hypothesis for why this might be is because we are splitting the diffusion and reaction terms in our operator splitting, handling the diffusion first. It is possible that some of the diffusion behavior might become lost when the scheme does not include the diffusion term. Although Bernasconi does not report the specific value for the period with diffusion, the figure they include seems to agree with the Euler scheme, with a period of just below 0.6 seconds.

Next, we recorded the positions on the ring of the activator peaks over all time. Since we wish to see the golden angle appear between activator peaks, this is where we might first determine the accuracy of our predictions.

In Figure 11 we can see that, once again, the Euler scheme seems to have predicted the behavior we desire. After about 13 seconds, the positions on the ring of the activator peaks seem to be separated by a constant amount. This is exactly the behavior Bernasconi describes, so next we hope to find that the distance between consecutive peaks converges to the golden angle. As before, the RK4 schemes seem to agree with one another in that most of the points seem to be at positions 0.7 and 0.4 on the ring. Once again, this could be an indicator that diffusion is not being properly

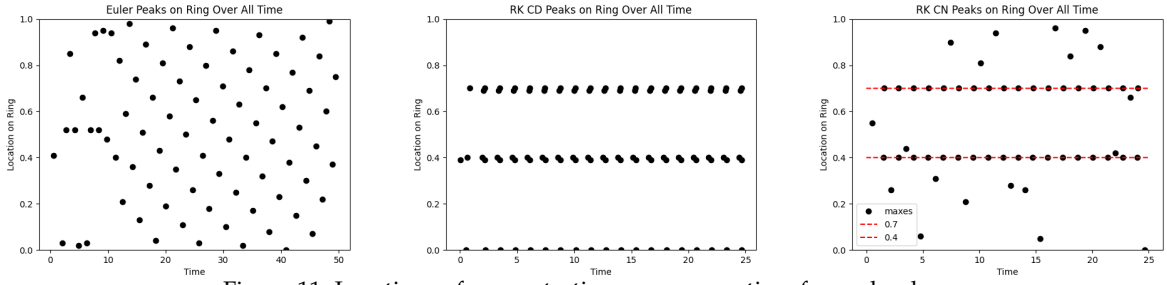

Figure 11: Locations of concentration maxes over time for each scheme

modeled in the scheme.

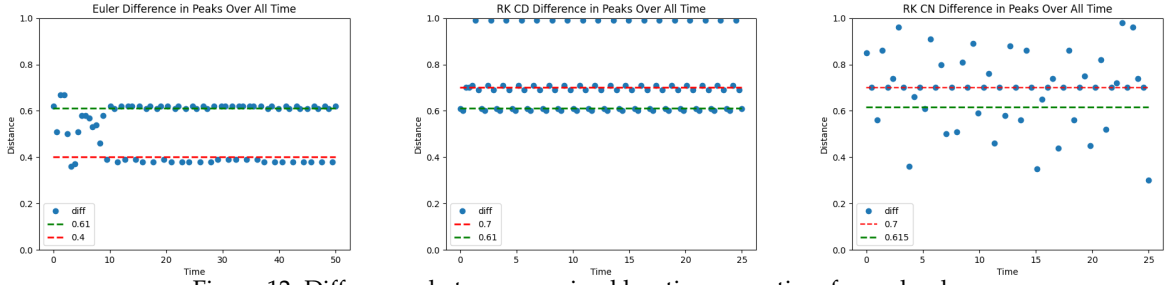

Figure 12: Differences between maximal locations over time for each scheme

To find the divergence angle, which should correspond to the golden angle, we need to find the distance between consecutive activator peaks. Since we are working with a unitary ring, these correspond directly to the arc length between the two points.

In Figure 12, we plot the difference between consecutive activator peaks over all time. Bernasconi reported that this value converged to a value between 0.61 and 0.62. While none of our schemes seem to converge to one value, both the Euler and RK4 with Central Difference seem to have many values around the 0.61 line. This is a good sign, though it is interesting that the Euler prediction in Figure 11 is so accurate and the RK4 CD is not, yet they both seem to exhibit the behavior we desire. It is also interesting to note that in Figure 11, we can see the strong preference for locations 0.4 and 0.7 in both RK4 schemes. However, it seems that the additional points in the RK4 with Crank Nicolson prediction not at the x=0 location (as they are in RK4 CD) were sufficient to result in almost no divergence angle equal to 0.6. Alternatively, they both have a consistent divergence angle of 0.7.

These results seem to indicate that the RK4 schemes may have been able to predict the simple oscillatory behavior of the activator, inhibitor, and source, but that the more nuanced behavior behind these oscillations was not as simply predicted using these methods.

3.5 Step Size Refinement

Next, as a suggestion from Professor Rycroft, we investigated whether refining the space step size could result in more accurate predictions for the divergence angle in the RK4 schemes. We simplified the code to only keep track of the activator predictions to save space, and refined our space step down to 0.0001. Since these schemes converged very quickly to the behavior detailed

above, we also shrunk our time interval down to just 10 seconds. Figure 13 shows the predictions of the RK4 Central Difference and RK4 Crank Nicolson schemes with this refined step size and a time step of 0.01 (again to save space).

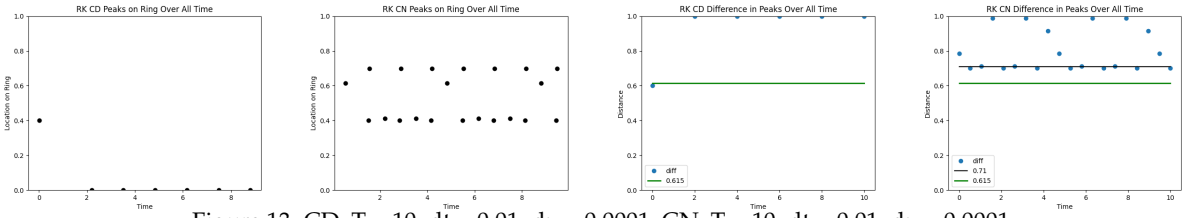

Figure 13: CD: T = 10, dt = 0.01, dx = 0.0001; CN: T = 10, dt = 0.01, dx = 0.0001

Noticeably, these predictions seem to be worse in the case of the Central Difference scheme, and to have made no significant difference in the Crank Nicolson scheme. Even though they are not pictured, the predictions for the concentration peaks and period remain unchanged, with maxima consistently reaching about 2, and a period of 1.32 seconds. This behavior is puzzling, because if it were a stability issue in the RK4 CD scheme causing these results, it would surely appear in the concentration predictions, yet it does not. Once again, we believe there is something wrong with the incorporation of diffusion in the schemes, but we were not able to investigate further in the allotted time.

4 Schnakenberg Reaction Diffusion System

In nature, spatial patterns form from homogeneous tissue resulting in different structures in different areas. Pattens in the morphogens in the initial tissue are thought to cause the patterns in structures [12]. There is debate over what causes these patterns in the initial tissue:

1. Auto and cross catalysis i.e. the products of activation and deactivation amplifying the activation rate [13],
2. polar cells, cells at the ends of the tissue, pumping morphogens or growth signalling molecules in one direction [14],
3. and the phase difference of two periodic events [15].

In this model and the following model we focus on (1). Additionally, there are a variety of ways to represent the reaction-kinetics, or the rate of chemical reactions, of a system. In this system we use Schnakenberg kinetics. In this Schnakenberg system we track the concentrations of an active signaling protein and an inactive signaling protein. We track the concentrations of proteins rather than hormones because we work on the cellular level. The same dynamics apply to activator and inhibitor hormones.

Within a cell, these proteins gather in specific areas and cause growth in that location. The active protein functions on a much shorter range while the inactive protein acts on a larger range [8]. A structure, such as a root hair, starting to grow in a location can be attributed to the active protein, and a hair not growing in a spot because it is too close to an already existing hair can be attributed to the long range inactive protein [12]. The active protein works in a smaller area, just

where the leaf is growing, while the inactive protein works on a larger range relating the positions of different leaves to each other [12]. Looking on the cellular level, active signaling proteins are more tightly bound to the cell membrane compared to the inactive proteins [8]. This leads to a slower diffusion rate and smaller range for active proteins.

Additionally, active and inactive signaling proteins react auto and cross catalytically which requires non-linear equations to describe their interaction [12]. The key difference between the Schnakenberg and Meinhart-Gierer kinetics is the non-linear term. The Schnakenberg model has a simpler non-linear term compared to the Meinhart-Gierer model presented later.

Here, the density of the structure protein is distinguished from the concentrations of the active and inactive signaling proteins. The structure protein has strong effects on growth patterns and is crucial to the system. The structure protein is distinct from a source that is used in other reaction diffusion models, but has similar impacts on the system.

4.1 Schnackenberg Reaction Diffusion Model with Linear Domain Growth

We use the Schnackenberg system given in [8]. The model is governed by the equations

$$\frac{\partial A}{\partial t} = D_A \frac{\partial^2 A}{\partial x^2} + k_1 I + k_2 s(x) A^2 I - (c + r) A \tag{14}$$

$$\frac{\partial I}{\partial t} = D_I \frac{\partial^2 I}{\partial x^2} - k_1 I - k_2 s(x) A^2 I + cA + b. \tag{15}$$

The state variables in the model are $A(x,t)$ and $I(x,t)$ which are defined as the overall concentration of the active proteins and inactive proteins, respectively.

Additionally, the model parameters are given in table 2.

Parameter	Definition
D_A	diffusion coefficient for the active proteins.
D_I	diffusion coefficient for the inactive proteins.
k_1	activation rate.
k_2	activation rate related to auto-catalysis.
$s(x)$	spatial distribution of the structure protein.
c	deactivation rate.
r	rate at which the activator is used up.
b	production rate of inactive proteins.
L_0	cell length at the time of growth initiation.

Table 2: Parameter Definitions for the Reaction Diffusion Model with Schnakenberg Reaction Kinetics and Linear Domain Growth.

Further, the graphic in Figure 14 depicts the basic dynamics of the Schnakenberg reaction diffusion system.

The first term of the RHS of both equations is the diffusion term, and is represented in the graphic by the loops labeled D_A and D_I. When the second spatial derivative is large and positive for a particular location, proteins are moving into that region and the concentration will increase. We assume here that $D_A << D_I$ so that the active proteins diffuse more slowly than the inactive

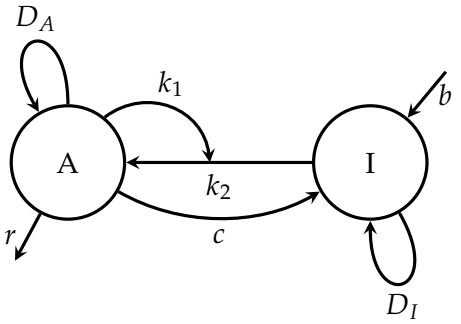

Figure 14: Diagram of the basic dynamics involved in the reaction diffusion system.

proteins, which is consistent with the spatial range relationships between active and inactive signaling proteins described earlier.

The second term in both equations describes the activation rate of these proteins. In the diagram, it is the arrow labeled k_2 that indicates the transfer of proteins from the inactive to active state. The third describes the auto and cross catalysis. A high concentration of both active proteins and inactive proteins leads to an even faster activation of inactive proteins. This is depicted in the diagram by the curving arrow labeled k_1. The terms with cA describe the deactivation rate and are illustrated by the arrow from A to I labeled c in the diagram. The term rA incorporates the rate at which active proteins are used up. They are no longer active or inactive proteins, so we depict it with the arrow r leaving the system. Finally, the term b is the production rate of inactive proteins. Other models like this contain a production rate of active proteins, but for our case we set this to be zero.

A good application of the Schnakenberg model is the growth of hairs on plant roots. Here we look in one dimension of space in a single cell since the longitudinal axis of a root cell is the most important in hair formation [8]. Reasonable parameter values for this type of system are given in Table 3.

Parameter	Value
D_A	0.1 $\mu m^2 s^{-1}$
D_I	10 $\mu m^2 s^{-1}$
k_1	0.01 s^{-1}
k_2	0.1 conc.$^2 s^{-1}$
$s(x)$	$e^{-1.5x/L_0}$
c	0.1 s^{-1}
r	0.01 s^{-1}
b	0.01 conc.s^{-1}
L_0	50 μm

Table 3: Parameter values and dimensions for the Schnakenberg model of root hair formation. These values are from [8].

Here conc. is the unit of concentration. Additionally, we use homogeneous initial conditions for the concentrations of the active and inactive proteins. We use zero-flux boundary conditions which means the proteins cannot diffuse through the cell wall [16].

For the finite difference methods implemented below, we use the spatial step $\Delta x = 0.1$ and the time step $\Delta t = \frac{0.4(dx)^2}{D_I}$ to ensure we satisfy the CFL conditions. For the spectral method, we use the same step in time defined by $\Delta x = 0.1$, and the same number of points in the domain at the initial time, but we use Chebyshev points.

We solve the system on the spatial domain from 0 to L, but the value of L changes with time as the cell expands after the proteins gather in one spot to form a hair. Once the cell begins to grow, it expands at a rate of 1 μm every 100 seconds. For the finite difference methods, since there is equal spacing between points, we know how many time steps will occur before the cell expands by

one spatial step. So, after the first 15 minutes when the cell is not growing, we loop through each set of time steps on the same size domain and use the last update from the previous as the initial condition for the next.

4.2 Numerical Methods

4.2.1 Forward Euler

For the first discretization, we take a forward finite difference for the time derivative and a centered difference formula for the spatial second derivative. This gives the equations

$$\begin{aligned}
\frac{A_j^{n+1} - A_j^n}{\Delta t} &= D_A \frac{A_{j-1}^n - 2A_j^n + A_{j+1}^n}{(\Delta x)^2} + k_1 I_j^n + k_2 s(j\Delta x)(A_j^n)^2 I_j^n - (c+r)A_j^n, \\
\frac{I_j^{n+1} - I_j^n}{\Delta t} &= D_I \frac{I_{j-1}^n - 2I_j^n + I_{j+1}^n}{(\Delta x)^2} - k_1 I_j^n - k_2 s(j\Delta x)(A_j^n)^2 I_j^n + cA_j^n + b.
\end{aligned}$$

Here n and j are the current time and spatial step, respectively. Rearranging to get the equation for the next step in time we obtain

$$A_j^{n+1} = A_j^n + \Delta t \left(D_A \frac{A_{j-1}^n - 2A_j^n + A_{j+1}^n}{(\Delta x)^2} + k_1 I_j^n + k_2 s(j\Delta x)(A_j^n)^2 I_j^n - (c+r)A_j^n \right), \quad (16)$$

$$I_j^{n+1} = I_j^n + \Delta t \left(D_I \frac{I_{j-1}^n - 2I_j^n + I_{j+1}^n}{(\Delta x)^2} - k_1 I_j^n - k_2 s(j\Delta x)(A_j^n)^2 I_j^n + cA_j^n + b \right). \quad (17)$$

4.2.2 Crank–Nicolson

The Crank Nicolson method uses a forward finite difference in time, like forward Euler, but uses a half of a centered difference in space at the current time step and a half at the next time step.

$$\begin{aligned}
\frac{A_j^{n+1} - A_j^n}{\Delta t} &= D_A \left(\frac{A_{j-1}^n - 2A_j^n + A_{j+1}^n}{2(\Delta x)^2} + \frac{A_{j-1}^{n+1} - 2A_j^{n+1} + A_{j+1}^{n+1}}{2(\Delta x)^2} \right) + k_1 I_j^n + k_2 s(j\Delta x)(A_j^n)^2 I_j^n - (c+r)A_j^n, \\
\frac{I_j^{n+1} - I_j^n}{\Delta t} &= D_I \left(\frac{I_{j-1}^n - 2I_j^n + I_{j+1}^n}{2(\Delta x)^2} + \frac{I_{j-1}^{n+1} - 2I_j^{n+1} + I_{j+1}^{n+1}}{2(\Delta x)^2} \right) - k_1 I_j^n - k_2 s(j\Delta x)(A_j^n)^2 I_j^2 n + cA_j^n + b.
\end{aligned}$$

Since this is an implicit method, we must solve a linear system at each time step. To get this linear system we use a second derivative centered difference matrix $\mathbf{D}^{(2)}$.

$$\begin{aligned}
\mathbf{A}_{n+1} &= \mathbf{A}_n + \Delta t \left(\frac{D_A}{2}\mathbf{D}^{(2)}\mathbf{A}_n + \frac{D_A}{2}\mathbf{D}^{(2)}\mathbf{A}_{n+1} + k_1\mathbf{I}_n + k_2\mathbf{S}\mathbf{A}_n^2\mathbf{I}_n - (c+r)\mathbf{A}_n \right), \\
\mathbf{I}_{n+1} &= \mathbf{I}_n + \Delta t \left(\frac{D_I}{2}\mathbf{D}^{(2)}\mathbf{I}_n + \frac{D_I}{2}\mathbf{D}^{(2)}\mathbf{A}_{n+1} - k_1\mathbf{I}_n - k_2\mathbf{S}\mathbf{A}_n^2\mathbf{I}_n + c\mathbf{A}_n + b \right).
\end{aligned}$$

The matrix $\mathbf{D}^{(2)}$ is a tridiagonal matrix with $\frac{-2}{(\Delta x)^2}$ on the main diagonal and $\frac{1}{(\Delta x)^2}$ on the off-diagonals with the exception of the first and last rows to satisfy the no-flux boundary conditions. The first row has the form

$$\begin{bmatrix} \frac{-1}{(\Delta x)^2} & \frac{1}{(\Delta x)^2} & 0 & \dots \end{bmatrix},$$

and the last row as the form

$$\begin{bmatrix} \dots & 0 & \frac{1}{(\Delta x)^2} & \frac{-1}{(\Delta x)^2} \end{bmatrix}.$$

We can rearrange this form of the system to get

$$\begin{aligned} \mathbf{A}_{n+1} - \frac{D_A \Delta t}{2}\mathbf{D}^{(2)}\mathbf{A}_{n+1} &= \mathbf{A}_n + \frac{\Delta t D_A}{2}\mathbf{D}^{(2)}\mathbf{A}_n + \Delta t\left(k_1\mathbf{I}_n + k_2\mathbf{S}\mathbf{A}_n^2\mathbf{I}_n - (c+r)\mathbf{A}_n\right), \\ \mathbf{I}_{n+1} - \frac{\Delta t D_I}{2}\mathbf{D}^{(2)}\mathbf{A}_{n+1} &= \mathbf{I}_n + \frac{\Delta t D_I}{2}\mathbf{D}^{(2)}\mathbf{I}_n + \Delta t\left(-k_1\mathbf{I}_n - k_2\mathbf{S}\mathbf{A}_n^2\mathbf{I}_n + c\mathbf{A}_n + b\right). \end{aligned}$$

Linear algebra techniques are used to solve for the next steps. Since these are tri-diagonal matrices, we exploit the sparsity of the matrices by using the `sparse()` function in MATLAB. Then, when we utilize the backslash operator to solve the matrix equation, it will automatically use more efficient techniques for the sparse matrix.

4.2.3 Spectral Method

For the time step we use the fourth order Runge-Kutta Method that uses the Butcher tableau

0				
2/5	2/5			
3/5	−3/20	3/4		
1	19/44	−15/44	40/44	
	11/72	25/72	25/72	11/72

This means we evaluate the right-hand sides of Equations 14 and 15 at the points specified in equations 18-21 to obtain the coefficients

$$\begin{aligned} r_1 &= RHS\left(\mathbf{U}_n\right) && (18) \\ r_2 &= RHS\left(\mathbf{U}_n + \frac{2\Delta t r_1}{5}\right) && (19) \\ r_3 &= RHS\left(\mathbf{U}_n + \frac{-3\Delta t r_1}{20} + 3\Delta t r_2 4\right) && (20) \\ r_4 &= RHS\left(\mathbf{U}_n + \frac{19\Delta t r_1}{44} + -15\Delta t r_2 44 + 40\Delta t r_3 44\right). && (21) \\ & && (22) \end{aligned}$$

Here $\mathbf{U}_n$ is either $\mathbf{A}_n$ or $\mathbf{I}_n$. We then use these coefficients to obtain the next guess for the next step by evaluating

$$\mathbf{U}_{n+1} = \mathbf{U}_n + \Delta t \left(\frac{11}{72} r_1 + \frac{25}{72} r_2 + \frac{25}{72} r_3 + \frac{11}{72} r_4 \right)$$

To obtain the RHS, we use the square of the non-periodic spectral derivative matrix presented in class. We only model $0 < x < L$, but when computing the matrix we include the boundaries. Since we are using no-flux boundary conditions, we remove the first and last rows and columns before squaring the matrix.

Once the domain begins to expand, we add another grid point at the same rate as the finite difference method using the theoretical $\Delta x = 0.2$ to determine that threshold. Since the spectral derivative matrix uses Chebyshev points, when expanding the domain, all of the points in the domain shift. This means we cannot use the previous step to compute the next step. To account for this, we interpolate the solution from the previous step and use that polynomial to compute the solution at the new points.

In order for the spectral method to be stable, the time step must satisfy $\Delta t < \frac{1}{D_I \|\lambda_{max}\|}$. Thus, we use a time step of size $\frac{0.4}{D_I \|\lambda_{max}\|}$ [17]. In this case, $\lambda_{max} = 5.05(10^4)$ and then the total number of time steps to produce just the first fifteen minutes of the simulation is $1.14(10^9)$. Based off of the rate at which it computes the first $100,000$ time steps, the first half of the simulation will take about six days to simulate and thus the total simulation will take at least twelve days. Since the simulation requires such long run times, we were unable to produce the result from simulation within the time frame of this project. However, the code is included in the Github link.

4.2.4 Results

Table 4 displays the run times for the different methods. The Forward Euler method is a little less than two times faster than the Crank Nicolson method. However, we know from class the Crank-Nicolson method has faster error convergence than the Forward Euler method. Additionally, the Crank Nicolson method does not need to satisfy the CFL condition for stability in theory. So, to reduce the computation time of a similar problem, one could increase the time step size.

As mentioned in Section 4.2.3, the run time for the spectral method is much longer due to the more strict stability conditions. For this reason, we do not have simulation results for this method. We were able to estimate the total run time from the part of the simulation we did run. While this problem does not require such a computationally expensive method, closely related systems do. In Section 4.3 we expand upon one of these examples to highlight the strengths of this method.

The solutions produced by these methods are indistinguishable as shown in Figure 15. In the plot, 0 represents the basal end of the cell. The active protein concentration peaks in this area, indicating our methods accurately reproduce the correct location of root hair growth.

4.3 A Note on the Schnakenberg Reaction Diffusion Model with Exponential Domain Growth

A variation of the Schnakenberg model presented above is the case when the domain length increases exponentially over time. When the growth rate is sufficiently fast, the number of peaks doubles [18]. The rate of domain growth is critical in producing the mode doubling pattern. If the rate of growth is too high and too close to the fast time scale at which the active and inactive protein concentrations vary, then we no longer see the mode doubling behavior. If the growth rate

Method	Run time
Forward Euler	11.7 sec
Crank-Nicolson	18.7 sec
Spectral	$\approx$ 12 days

Table 4: Wall clock run times for the three different numerical methods implemented to solve the Schnakenberg reaction diffusion system.

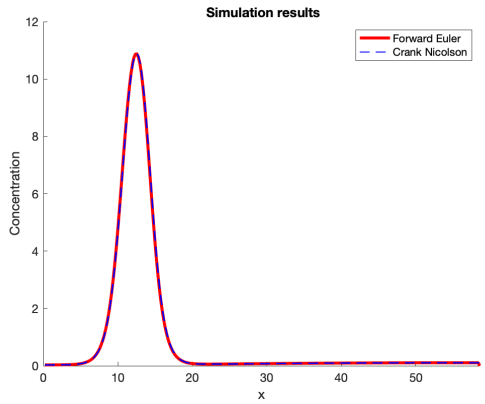

Figure 15: Schnakenberg model solved using the Forward Euler and Crank Nicolson methods. Here the solutions to the activator concentrations are plotted at $t = 30$ minutes.

is too small the doubling mode behavior should still occur, but with some numerical methods it does not [18]. Specifically, [18] finds that using a spectral method captures this mode doubling while the finite difference method does not.

An example system is given in Equations 23 - 25.

$$\frac{\partial A}{\partial t} = \frac{d}{L^2}\frac{\partial^2 A}{\partial x^2} - IA^2 + a - \rho A \tag{23}$$

$$\frac{\partial I}{\partial t} = \frac{1}{L^2}\frac{\partial^2 I}{\partial x^2} - IA^2 + b - \rho I \tag{24}$$

$$\frac{dL}{dt} = \rho L \tag{25}$$

Compared to the prior Schnakenberg model, we see some new parameters and some missing parameters. d is the new diffusion coefficient for active proteins, a is the production rate of active proteins, and ρ is the growth rate of the domain.

There are many places in nature where this mode splitting pattern emerges, such as pigmentation in fish [18]. Thus, it is a relevant dynamic to study. This example highlights the usefulness of spectral methods in solving these systems, despite the longer run time.

5 Conclusion and Future Work

The mathematical study of botanical phenomena is an amazingly rich field of research, and there is plenty of further work we could pursue. In particular, we could

- Study the physical perspective for phyllotaxis proposed by Doaudy and Couder in depth;
- Investigate growth rates and phyllotactical results for various plants, as Tanaka's model included parameters that specified the growth rate of one particular plant (and the divergence angle's convergence to Φ was dependent on these parameters);

- Reproduce the results of the Tanaka model using other numerical methods;
- Upgrade the Tanaka Solver in C++ to increase efficiency and compare the timing results to the MATLAB timing data;
- Further investigate whether the diffusive behavior of the Bernasconi system is lost in the RK4 schemes;
- Correct the Newton's method code for a fast and accurate prediction of the Bernasconi system using a method that works especially well for nonlinear systems, which will hopefully make accurate predictions for each part of the model;
- Run the spectral method for the Schnakenberg system for the full simulation time compare results against those for the finite difference methods;
- Apply the spectral method presented here, and other unexplored methods, to the Schnakenberg model with exponential domain growth.

5.1 Acknowledgments

We would like to express our gratitude to Professor Chris Rycroft and the UW-Madison math department for a great semester. This has been an extremely useful course and we are looking forward to utilizing the skills we've learned in the future. Thank you!

References

[1] Phyllotaxis, Wikipedia (2024).

[2] H. Meinhardt, Models of biological pattern formation: From elementary steps to the organization of embryonic axes, in: Current Topics in Developmental Biology, Current topics in developmental biology, Elsevier, 2008, pp. 1–63.

[3] W. F. B. Hofmeister, Allgemeine Morphologie der Gewächse, Leipzig, W. Engelmann, 1868.

[4] A. C. Newell, M. Pennybacker, Fibonacci patterns: Common or rare?, Procedia IUTAM 9 (2013) 86–109. URL https://api.semanticscholar.org/CorpusID:84763631

[5] Y. Tanaka, A reaction diffusion model for understanding phyllotactic formation, Japan Journal of Industrial Applied Math 33 (2016) 183–205. doi:10.1007/s13160-015-0202-8.

[6] D. Reinhardt, Regulation of phyllotaxis by polar auxin transport, Nature (2003) 255–260doi:10.1038/nature02081.

[7] G. S. M. T. R. D. K. C. P. P. Smith, R.S., A plausible model of phyllotaxis, Proceedings of the National Academy of Sciences (2006) 1301–1306.

[8] R. J. Payne, C. S. Grierson, A theoretical model for rop localisation by auxin in arabidopsis root hair cells, PLoS One 4 (12) (2009) e8337.

[9] V. F. Breña-Medina, Dynamical features of a biochemical interaction in a plant root hair cell: A long story short, Quantitative Models for Microscopic to Macroscopic Biological Macromolecules and Tissues (2018) 189–215.

[10] G. Bernasconi, Reaction-diffusion model for phyllotaxis, Physica D: Nonlinear Phenomena 70 (1) (1994) 90–99. doi:https://doi.org/10.1016/0167-2789(94)90058-2.

[11] H. J. Scholz, Phyllotactic iterations, Ber. Bunsenges. Phys. Chem. 89 (6) (1985) 699–703.

[12] A. Gierer, H. Meinhardt, A theory of biological pattern formation, Kybernetik 12 (1972) 30–39.

[13] A. M. Turing, The chemical basis of morphogenesis, Bulletin of mathematical biology 52 (1990) 153–197.

[14] P. A. Lawrence, Gradients in the insect segment: the orientation of hairs in the milkweed bug oncopeltus fasciatus, Journal of Experimental Biology 44 (3) (1966) 607–620.

[15] B. C. Goodwin, M. H. Cohen, A phase-shift model for the spatial and temporal organization of developing systems, Journal of Theoretical Biology 25 (1) (1969) 49–107.

[16] V. Brena-Medina, A. R. Champneys, C. Grierson, M. J. Ward, Mathematical modeling of plant root hair initiation: Dynamics of localized patches, SIAM Journal on Applied Dynamical Systems 13 (1) (2014) 210–248.

[17] L. N. Trefethen, Spectral methods in MATLAB, SIAM, 2000.

[18] I. Barrass, E. J. Crampin, P. K. Maini, Mode transitions in a model reaction–diffusion system driven by domain growth and noise, Bulletin of mathematical biology 68 (2006) 981–995.